



## Research Article

# Cross-Receiver Open-Set Radio Frequency Fingerprinting via Structure-First Adaptation

Fengchong YAO<sup>1</sup>, Jianbing LI<sup>†1</sup>, Qing LIU<sup>1</sup>, Kefeng SONG<sup>1</sup>, Haitao LI<sup>1</sup>, Song WANG<sup>1</sup>, Feixiang WANG<sup>1</sup>

<sup>1</sup>School of Information Systems Engineering, Information Engineering University, Zhengzhou 450001, China

<sup>†</sup>E-mail: li\_jb@126.com

**Abstract:** Radio frequency fingerprint identification (RFFI) provides a physical-layer credential for Internet of Things devices, but open-set decisions become fragile when a threshold calibrated on a source receiver is applied to a target receiver. Receiver shift can lower the confidence of known transmitters and cause false rejection, whereas closed-set alignment can pull unseen target transmitters into known regions and increase false acceptance. This paper presents a Cross-Receiver Open-set Domain Adaptation framework via Structure-first Training (CRODA-ST) for RFFI. Discriminative Structure Anchoring (DSA) restores target-receiver known-class references from limited labeled target enrollment samples, and Rejection-Oriented Alignment (ROA) reduces receiver-sensitive confidence fluctuations around the anchored structure. On the WiSig ManyTx dataset, CRODA-ST achieves 0.9092 known-class accuracy, 0.9692 area under the receiver operating characteristic curve (AUROC), 0.9580 open-set classification rate (OSCR), and a false positive rate of 0.0469 at a 90% true positive rate (FPR<sub>90</sub>). Additional evaluations on a controllable LoRa simulation dataset examine the method under synthesized hardware distortions.

**Key words:** Radio frequency fingerprint identification; cross-receiver transfer; open-set recognition; domain adaptation

**CLC number:** TN

## 1 Introduction

Radio frequency fingerprint identification (RFFI) provides a critical physical-layer credential for Internet of Things (IoT) security by authenticating wireless devices through hardware-induced transmitter impairments (Zhang et al., 2023). In practical deployments, this credential must satisfy two strict criteria: it must remain reliable despite receiving hardware variations, and it must decisively reject traffic from unregistered devices.

However, existing methods typically evaluate RFFI under an idealized closed-system assumption, whereas real-world deployments suffer from severe condition mismatches. As shown in Fig. 1, an operational authentication system routinely encounters

both registered and unregistered devices, while capturing signals across physically dispersed, heterogeneous receivers. These receivers introduce localized distortions—such as variations in local oscillators, sampling clocks, and RF front-end filters—that continuously shift the in-phase/quadrature (I/Q) feature manifold (Hanna et al., 2022; Shen et al., 2024; Li et al., 2025; Ma et al., 2025a). Consequently, RFFI is fundamentally a cross-receiver transfer and unknown-device rejection problem, not merely a static closed-set classification task.

Although prior research has made significant progress in domain adaptation and open-set recognition, these challenges are typically isolated under mutually exclusive assumptions. Existing cross-receiver methods often assume a strictly closed-set label space, inadvertently classifying unknown transmitters into registered identities. Conversely, cur-

<sup>†</sup> Corresponding author

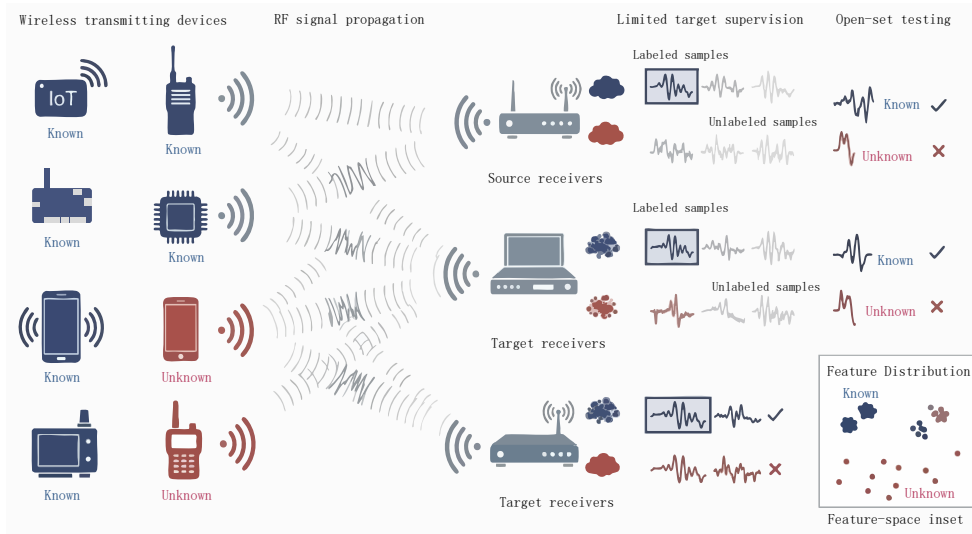


**Fig. 1** Application scenario of cross-receiver open-set radio frequency fingerprint identification.

rent open-set methods evaluate rejection capabilities without accounting for strong receiver shifts (Hanna et al., 2022; Ma et al., 2025a; Huang et al., 2025; Hong et al., 2026). This theoretical division breaks down in practical IoT authentication, where a deployed receiver simultaneously observes shifted known features and entirely novel unknown identities.

To bridge this gap, this paper investigates the single-source single-target cross-receiver open-set setting. In this strict deployment protocol, unknown target transmitters are entirely excluded from the training, threshold calibration, and model selection phases. The rejection decision must rely exclusively on source-calibrated validation scores. This rigid calibration exposes two contrasting failure modes in deep neural networks. First, receiver shift depresses the confidence scores of target-known samples, causing **false rejection** of registered devices. Second, naive closed-set domain alignment indiscriminately pulls unseen target transmitters into known clusters, causing **false acceptance** of unregistered traffic.

Therefore, we approach this task not as standard domain adaptation, but as a source-calibrated threshold reliability problem. To this end, we propose the CRODA-ST framework, which introduces a structure-first feature alignment mechanism. The framework explicitly reconstructs target-known reference points through Discriminative Structure Anchoring (DSA), and subsequently

stabilizes receiver-sensitive confidence boundaries via Rejection-Oriented Alignment (ROA). Unlike generic adaptation networks that optimize solely for classification accuracy, CRODA-ST explicitly engineers the intermediate representation space. This structural design ensures that the source-calibrated maximum softmax probability (MSP) threshold remains reliable under severe receiver shift.

To complement the extensive WiFi empirical measurements, we additionally evaluate the proposed architecture on a synthesized Chirp Spread Spectrum (CSS) LoRa dataset. This cross-protocol validation examines whether the same source-calibrated open-set formulation remains usable under systematically controlled transmitter and receiver hardware impairments.

This work makes three main contributions.

1) *Problem formulation*: We define the single-source single-target cross-receiver open-set RFFI problem under strict source-only threshold calibration. We demonstrate that shifted known samples and unseen transmitters induce opposing threshold errors, explicitly separating threshold reliability from standard closed-set calibration.

2) *Method design*: We propose CRODA-ST, integrating DSA and ROA into a unified training flow. The DSA module anchors target-known spatial references using limited enrollment data, while the ROA module regularizes the shared posterior bounds to suppress unknown overlap without requiring target-

unknown exposure.

3) *Experimental verification:* We systematically validate the framework on the WiSig ManyTx dataset, where CRODA-ST achieves a 0.9580 open-set classification rate (OSCR) while reducing false acceptance. Additional evaluations on a controllable LoRa simulation array provide a cross-protocol check under synthesized hardware distortions.

The remainder of this paper is organized as follows. Section 2 reviews RFFI-based IoT authentication, cross-receiver transfer, and open-set recognition, positioning the proposed setting relative to existing paradigms. Section 3 formulates the cross-receiver open-set problem and details the DSA and ROA mechanisms of CRODA-ST. Section 4 reports the experimental protocol, comparative analysis, ablations, and specialized evaluations on the LoRa array. Section 5 concludes the paper.

## 2 Related Work

### 2.1 Radio Frequency Fingerprint Identification

Radio Frequency Fingerprint Identification (RFFI) provides a physical-layer authentication mechanism by exploiting hardware-intrinsic imperfections in the radio-frequency front end of transmitters (Zhang et al., 2023; Sa et al., 2019; Yan et al., 2025). As wireless devices are increasingly deployed in open IoT environments, RFFI has become an essential supplement to cryptographic protocols, offering spoofing-resistant and lightweight device verification (Peng et al., 2019; Cai et al., 2024; Qi et al., 2024). Traditional feature engineering and deep learning models have achieved promising classification accuracy under controlled same-domain scenarios, where the propagation channel and receiver hardware remain stable (Wang et al., 2025b; Shen et al., 2022; Xing et al., 2023; Peng et al., 2024). However, practical deployment conditions are far from ideal. Real-world IoT systems often involve diverse receiver hardware, changing acquisition environments, and unpredictable environmental noise (Hanna et al., 2022; Chillet et al., 2024). Such hardware and environmental variations induce significant distribution shifts, causing representations learned under ideal assumptions to transfer poorly and hindering the practical deployment of RFFI.

### 2.2 Cross-Receiver and Domain Adaptation in RFFI

To mitigate the deployment mismatch caused by hardware variations, cross-receiver RFFI has been formulated as a domain shift problem. Prior studies address receiver-induced differences through domain adaptation, feature transformation, or domain generalization. For example, adversarial training and contrastive alignment have been used to extract receiver-invariant representations (Shen et al., 2024; Ma et al., 2025a; Zhang et al., 2025; Zha et al., 2023). Other strategies incorporate feature transformation, pseudo-label self-training, and multi-objective domain adaptation to stabilize target-domain alignment (Yang et al., 2024; Xiao et al., 2025; Yang et al., 2025b; Feng et al., 2025).

Although these cross-receiver methods effectively mitigate hardware-induced domain shifts, their effectiveness is fundamentally constrained by the closed-set assumption. They implicitly assume that the source and target domains share identical label spaces. In open IoT environments, however, the target domain inevitably encounters unregistered or rogue devices. Forcing distribution alignment under a closed-set formulation can maliciously map unknown device features into known-class regions, leading to severe false acceptance and undermining the core security objective of RFFI.

### 2.3 Open-Set RFFI

Recognizing the limitations of closed-set classifiers, open-set recognition (OSR) requires the model to correctly classify known devices while robustly rejecting unknown classes absent during training (Bendale and Boulton, 2016; Geng et al., 2021; Chen et al., 2021). In the context of RFFI, recent methods improve unknown-class rejection using metric-enhanced autoencoders, prototype learning, out-of-distribution exposure, and test-time calibration (Huang et al., 2025; Wang et al., 2025a; Xing et al., 2025; Huang et al., 2024; Ma et al., 2025b; Kangsheng et al., 2026).

While these open-set methods excel at rejecting rogue devices under stable conditions, most of them are evaluated under the same receiver or weak domain shifts. In cross-receiver deployments, hardware-induced feature drift distorts both the known-class boundaries and the source-calibrated

confidence distributions. Consequently, existing rejection mechanisms—such as distance thresholds or prototype matching—become unreliable when directly transferred to a new receiver. Similarly, while unknown-aware alignment strategies have been studied in general open-set domain adaptation (Gao et al., 2020; Loghmani et al., 2020; Wang, 2021; Zhao et al., 2023), they have not been systematically tailored to suppress receiver-specific hardware artifacts in RFFI.

## 2.4 Open-Set Recognition Across Receivers

A small number of pioneer studies have begun to jointly model cross-domain transfer and open-set rejection. For instance, Hong et al. explored cross-domain open-set RFFI through pseudo-label learning and prototype calibration (Hong et al., 2026). Generative auxiliary modeling and multi-task discrimination have also been introduced to combine feature alignment with open-set robustness (Guo et al., 2024; Yang et al., 2025a).

Different from approaches that require abundant target-domain data or complex generative models, this work focuses on a highly constrained yet realistic scenario: cross-receiver open-set recognition with only limited labeled target-domain data and source-only threshold calibration. In this setting, the model must simultaneously form a well-clustered target-domain known-class structure and maintain a stable, source-calibrated open-set boundary against receiver shifts. These stringent constraints and deployment demands directly motivate the design of the proposed method.

## 3 Proposed Method

### 3.1 Problem Formulation and Design Rationale

We formulate single-source single-target cross-receiver open-set RFFI as a source-calibrated rejection problem. The source receiver provides labeled known-class samples  $\mathcal{D}_s = \{(x_i^s, y_i^s)\}_{i=1}^{n_s}$ , where  $y_i^s \in \mathcal{Y}_K = \{1, \dots, K\}$  denotes a registered transmitter. The target receiver provides a limited labeled target enrollment set  $\mathcal{D}_t^l = \{(x_j^t, y_j^t)\}_{j=1}^{n_t}$  from the same known transmitter set (e.g., 20 samples per class). This small enrollment budget models a practical low-cost device onboarding protocol in IoT deployment,

requiring only a few milliseconds of I/Q signal capture per device during physical registration. Unknown target identities  $\mathcal{Y}_U$  satisfy  $\mathcal{Y}_K \cap \mathcal{Y}_U = \emptyset$  and appear only during testing; no target-unknown sample is used for training, threshold calibration, hyperparameter tuning, or model selection.

This protocol differs from ordinary closed-set adaptation because the final target decision depends on a Maximum Softmax Probability (MSP) threshold calibrated only from source known samples. The method must therefore keep shifted target-known samples compatible with the source-calibrated known-class structure; otherwise, the threshold rejects registered transmitters for receiver-related rather than identity-related reasons. At the same time, adaptation must not use target-unknown samples or blindly align all target data, since such alignment may absorb unseen transmitters into known regions and increase false acceptance.

CRODA-ST follows this structure-first rationale. It converts each target test segment into either a known transmitter label or an unknown rejection, while training the same encoder–classifier path under two coupled constraints. Discriminative Structure Anchoring (DSA) uses labeled target enrollment samples to rebuild target-side references for registered transmitters before rejection is applied. Rejection-Oriented Alignment (ROA) regularizes receiver-sensitive embedding and posterior variations around this anchored known-class structure. The two parts are not trained as separate phases: each epoch jointly optimizes DSA losses and ROA regularizers on source samples and labeled target enrollment samples. DSA determines where known classes should lie under the target receiver, whereas ROA makes the MSP score less sensitive to receiver-induced fluctuations without changing the source-calibrated inference rule.

### 3.2 Input Representation and Encoder

The input is a complex baseband segment represented by in-phase and quadrature (I/Q) channels. Energy normalization mitigates sample-scale variation, and source-fitted standardization applies the same reference statistics to source training, target enrollment, source validation, and test samples. We write the resulting I/Q–time representation as  $x \in \mathbb{R}^{2 \times 256}$ .

A residual encoder  $b_\theta(\cdot)$  maps  $x$  to a back-

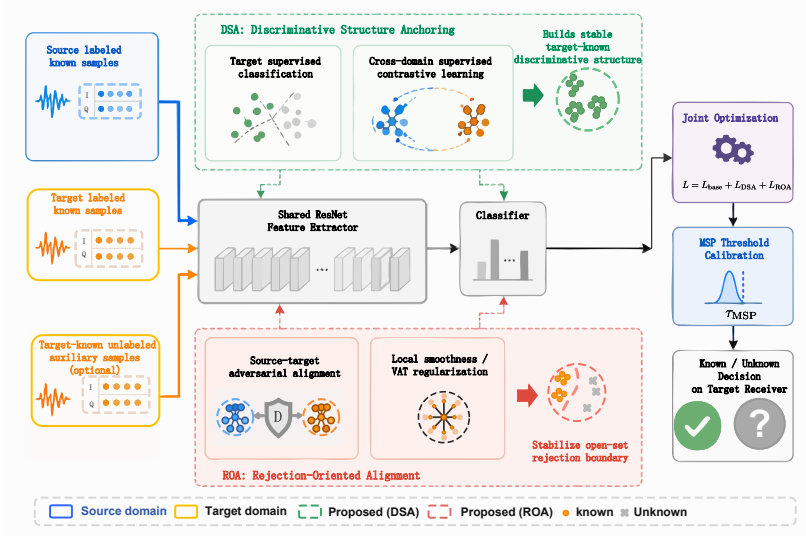


**Fig. 2** Overview of CRODA-ST. DSA restores target known-class references for source-calibrated thresholding, while ROA regularizes receiver-sensitive confidence fluctuations around the anchored structure. The optional target-known unlabeled auxiliary samples denote extra known-class target signals used only in the diagnostic few-shot variant; they are excluded from the main protocol, target CE, supervised contrastive learning, threshold calibration, and model selection, and no target-unknown samples are exposed.

bone feature that should preserve transmitter-discriminative structure while reducing sensitivity to receiver-dependent distortion. This role is important because the same representation supports known-class recognition and MSP-based rejection. The backbone feature is projected to the classifier embedding used by all downstream losses:

$$z = f_{\theta}(x) = W_p b_{\theta}(x) + b_p, \quad z \in \mathbb{R}^{128}. \quad (1)$$

A single linear  $K$ -way classifier then produces known-class logits and posteriors,

$$\ell(x) = W_c z + b_c, \quad p(x) = \text{softmax}(\ell(x)). \quad (2)$$

Thus, recognition and open-set scoring use the same 128-D embedding and the same linear classifier. CRODA-ST keeps the inference rule MSP-based, so its rejection gain is attributed to target-known anchoring and confidence regularization, not to post-hoc OpenMax recalibration or dummy unknown classes.

### 3.3 Discriminative Structure Anchoring

As illustrated in Fig. 2, DSA repairs the known-class side of the rejection problem before confidence regularization is applied. Source-calibrated rejection is meaningful only when the classifier's known-class

decision surface remains reliable for both the source receiver and the enrolled target receiver. Source mini-batches  $\mathcal{B}_s \subset \mathcal{D}_s$  keep this decision surface discriminative for registered transmitters:

$$\mathcal{L}_s = -\frac{1}{|\mathcal{B}_s|} \sum_{(x_i^s, y_i^s) \in \mathcal{B}_s} \log p_{y_i^s}(x_i^s). \quad (3)$$

Target enrollment mini-batches  $\mathcal{B}_t^l \subset \mathcal{D}_t^l$  use the same encoder and classifier. Their labels place receiver-shifted target known samples under the same output classes:

$$\mathcal{L}_t = -\frac{1}{|\mathcal{B}_t^l|} \sum_{(x_j^t, y_j^t) \in \mathcal{B}_t^l} \log p_{y_j^t}(x_j^t). \quad (4)$$

These two cross-entropy (CE) terms form the supervised part of DSA: source samples preserve the class decision surface, and labeled target enrollment samples repair the target side of that surface. Because both terms are averaged over their mini-batches, the unit target weight in the main objective treats scarce target enrollment samples as reliable class anchors rather than weak auxiliary data.

Class-level anchoring also needs an embedding-level constraint, because a correct logit label alone does not ensure that source and target samples of the same transmitter occupy a shared local structure. Source samples and labeled target enrollment

samples are merged as  $\mathcal{B}_{st} = \mathcal{B}_s \cup \mathcal{B}_t^l$ . Let  $\tilde{z} = z/\|z\|_2$ ,  $\mathcal{P}(i) = \{j : j \neq i, y_j = y_i\}$  be the positive set of anchor  $i$ , and  $\mathcal{A} = \{i : |\mathcal{P}(i)| > 0\}$ . The supervised contrastive loss is

$$\mathcal{L}_{\text{sup}} = -\frac{1}{|\mathcal{A}|} \sum_{i \in \mathcal{A}} \frac{1}{|\mathcal{P}(i)|} \sum_{j \in \mathcal{P}(i)} \log \frac{\exp(\tilde{z}_i^\top \tilde{z}_j / T_c)}{\sum_{a \in \mathcal{B}_{st} \setminus \{i\}} \exp(\tilde{z}_i^\top \tilde{z}_a / T_c)} \quad (5)$$

where  $T_c$  is a temperature scaling hyperparameter. This term pulls source and target embeddings of the same transmitter together while separating different transmitters. As a result, target-known samples acquire class structure before the MSP threshold is used for rejection.

### 3.4 Rejection-Oriented Alignment

As shown in the bottom branch of Fig. 2, after DSA supplies target known-class references, the main remaining risk is confidence instability around that structure. Receiver-dependent variations may still perturb the posterior  $p(x)$  and the MSP score near the rejection boundary. ROA addresses this part of the failure chain with two training-time constraints on the embedding and posterior, while leaving the inference path unchanged.

First, ROA penalizes receiver-identifiable variation in the normalized classifier embedding by using a receiver discriminator  $d_\phi(\cdot)$  with a Gradient Reversal Layer (GRL). Let  $q(x) = \text{softmax}(d_\phi(\text{GRL}(\tilde{z})))$  and let  $r(x) \in \{0, 1\}$  denote the receiver label (0 for source and 1 for target). The source–target receiver loss is

$$\mathcal{L}_{\text{dom}} = -\frac{1}{|\mathcal{B}_s| + |\mathcal{B}_t^l|} \sum_{x \in \mathcal{B}_s \cup \mathcal{B}_t^l} \log q_{r(x)}(x). \quad (6)$$

The discriminator learns receiver separation, whereas the gradient-reversed encoder learns to suppress receiver-discriminative cues (Ganin et al., 2016). This loss is deliberately restricted to source samples and labeled target enrollment samples. Target-unknown samples are unavailable during deployment calibration and, if used for blind receiver alignment, could be pulled toward the known source structure and weaken the open-set boundary. In the main single-source single-target setting, ROA therefore uses only this source–target known-sample alignment.

Second, Virtual Adversarial Training (VAT) regularizes the posterior locally around both source

and labeled target enrollment samples (Miyato et al., 2018). For each  $x \in \mathcal{B}_{st}$ , the current posterior  $p(x)$  is treated as a reference distribution. An adversarial perturbation  $r_{\text{adv}}$  is estimated with one power iteration,  $\xi = 10^{-6}$ , and radius  $\epsilon = 2.0$ . The smoothing

$$\mathcal{L}_{\text{vat}} = \frac{1}{|\mathcal{B}_{st}|} \sum_{x \in \mathcal{B}_{st}} D_{\text{KL}}(p(x) \| p(x + r_{\text{adv}})). \quad (7)$$

Here, the reference posterior  $p(x)$  is treated as fixed during backpropagation via a stop-gradient operator, updating parameters solely through the perturbed branch  $p(x + r_{\text{adv}})$ . Because the final rejection decision depends directly on MSP, this term discourages abrupt posterior changes around anchored known samples under small signal perturbations.

### 3.5 Optimization and Source-Calibrated Output

The complete objective anchors registered-transmitter structure across the two receivers while regularizing receiver-sensitive confidence changes around that structure. It combines the supervised anchoring terms with the two rejection-oriented regularizers, and all terms are optimized jointly in every training epoch:

$$\mathcal{L} = \mathcal{L}_s + \lambda_t \mathcal{L}_t + \lambda_c \mathcal{L}_{\text{sup}} + \lambda_d \mathcal{L}_{\text{dom}} + \lambda_v \mathcal{L}_{\text{vat}}, \quad (8)$$

where  $\lambda_t$ ,  $\lambda_c$ ,  $\lambda_d$ , and  $\lambda_v$  balance target enrollment anchoring, cross-receiver contrast, receiver suppression, and local posterior smoothness. The unit value of  $\lambda_t$  in the main experiments reflects the role of target CE as enrollment anchoring: the target labels are few but trustworthy, and down-weighting them would leave shifted target-known samples under the source decision surface. The remaining terms regularize this anchored structure instead of replacing supervised fingerprint discrimination.

At deployment, only the components needed for the source-calibrated decision rule are retained: the feature extractor, projection layer, linear classifier, MSP score, and threshold. Given the posterior  $p(x)$ , the knownness score and raw known-class prediction are

$$s(x) = \max_{k \in \mathcal{Y}_K} p_k(x), \quad \hat{k}(x) = \arg \max_{k \in \mathcal{Y}_K} p_k(x). \quad (9)$$

The threshold is estimated only from the source known-class validation set  $\mathcal{D}_{\text{val}}^s$ :

$$\tau = Q_{1-\rho}(\{s(x_i) : (x_i, y_i) \in \mathcal{D}_{\text{val}}^s\}), \quad (10)$$

---

**Algorithm 1** Source-calibrated optimization and inference of CRODA-ST.
 

---

- 1: **Input:** Known-class source set  $\mathcal{D}_s$ , labeled target enrollment set  $\mathcal{D}_t^l$ , source validation set  $\mathcal{D}_{\text{val}}^s$ , and retention rate  $\rho$ . (MSP: maximum softmax probability).
  - 2: **Output:** Encoder  $b_\theta(\cdot)$  with projection head  $f_\theta(\cdot) = W_p b_\theta(\cdot) + b_p$ , classifier head, and source-calibrated threshold  $\tau$ .
  - 3: **Joint DSA–ROA training.**
  - 4: **for** each epoch **do**
  - 5:   **for** mini-batches  $\mathcal{B}_s \subset \mathcal{D}_s$  and  $\mathcal{B}_t^l \subset \mathcal{D}_t^l$  **do**
  - 6:     Compute DSA terms  $\mathcal{L}_s$ ,  $\mathcal{L}_t$ , and  $\mathcal{L}_{\text{sup}}$  to anchor source and target known-class structure.
  - 7:     Compute ROA terms  $\mathcal{L}_{\text{dom}}$  and  $\mathcal{L}_{\text{vat}}$  on the same source and labeled target enrollment samples.
  - 8:     Update the shared encoder and classifier by minimizing  $\mathcal{L}_s + \lambda_t \mathcal{L}_t + \lambda_c \mathcal{L}_{\text{sup}} + \lambda_d \mathcal{L}_{\text{dom}} + \lambda_v \mathcal{L}_{\text{vat}}$ .
  - 9:   **end for**
  - 10: **end for**
  - 11: **Unknown-free threshold calibration.**
  - 12: Estimate MSP scores on  $\mathcal{D}_{\text{val}}^s$  and set  $\tau = Q_{1-\rho}(\{s(x_i) : (x_i, y_i) \in \mathcal{D}_{\text{val}}^s\})$ .
  - 13: **Deployment inference.**
  - 14: For a target test sample  $x$ , compute  $s(x)$  and  $\hat{k}(x)$ ; output  $\hat{k}(x)$  if  $s(x) \geq \tau$ , otherwise reject it as unknown ( $-1$ ).
- 

where  $Q_{1-\rho}(\cdot)$  returns the lower quantile that retains a prespecified fraction  $\rho$  of source validation known samples. This retention rate defines a preset source-side operating point: it accepts a fixed fraction of registered source users before any target-unknown identity is observed. In the experiments, all methods use the same calibration rule with  $\rho = 0.90$  for deployment-style open-set prediction, so the threshold is not tuned with target unknowns or post-hoc target feedback. Metrics such as  $\text{FPR}_{90}$  are computed separately by sweeping the same knownness score to the required TPR operating point. The final target output is

$$\hat{y}(x) = \begin{cases} \hat{k}(x), & s(x) \geq \tau, \\ -1, & s(x) < \tau, \end{cases} \quad (11)$$

where  $-1$  denotes rejection as an unknown transmitter. Algorithm 1 summarizes the source-calibrated optimization, calibration, and inference protocol.

## 4 Experimental Results and Analysis

### 4.1 Experimental Setup

We systematically evaluate the proposed CRODA-ST framework on the large-scale WiSig ManyTx WiFi baseband dataset (Hanna et al., 2022). This testbed provides heterogeneous receivers, many transmitters, and cross-day captures, enabling a rigorous protocol that mirrors real-world IoT deployment mismatches. Specifically, the set-

ting supports a main canonical transfer, 10 random source-target combinations, and temporal enrollment tests under strict unknown-free calibration. To complement these empirical WiFi evaluations, Section 4.6 extends the validation to a synthetic LoRa array to isolate performance under systematically controlled hardware impairments.

For data representation, each length-256 I/Q sample is centered, energy-normalized, standardized using source-training statistics, and formatted as a  $2 \times 256$  input tensor. The backbone architecture employs a 2-D residual I/Q-time encoder with 32 base channels, (2, 2, 2) residual blocks, and a 128-dimensional classification embedding. During optimization, we train the network using the Adam optimizer for 80 epochs. We set the batch size to 64, learning rate to  $10^{-3}$ , and weight decay to  $10^{-4}$  with cosine annealing. Unless otherwise specified, the hyperparameters are set as follows:  $\lambda_t = 1.0$ ,  $\lambda_c = 0.05$ ,  $T_c = 0.07$ ,  $\lambda_d = 0.1$ ,  $\lambda_v = 0.05$ ,  $\epsilon = 2.0$ , and the gradient reversal coefficient is 1.0.

To ensure a fair comparison, all baseline methods strictly share the same source split, labeled target enrollment budget, domain adaptation setting, and unknown-free calibration rule. Crucially, target-known labels are strictly withheld unless explicitly required by the baseline’s original objective. For instance, target-supervised MSP and target-supervised OpenMax utilize the exact same labeled target enrollment samples as CRODA-ST, but without the proposed DSA–ROA regularization. Finally, to rigorously test receiver-pair robustness, we average the results over 10 random source-target pairs, each spanning three dataset splits and three random seeds.

The reported evaluation metrics comprehensively capture the closed-set recognition and open-set rejection tradeoff: known-class accuracy ( $\text{Acc}_K$ ), area under the receiver operating characteristic curve (AUROC), open-set classification rate (OSCR), and the false positive rate at a 90% true positive rate ( $\text{FPR}_{90}$ ). Let  $\mathcal{D}_K$  and  $\mathcal{D}_U$  denote the known and unknown test sets, respectively. For a known test sample  $x$  and its ground-truth label  $y$ , let  $s(x)$  denote the knownness score,  $\hat{k}(x)$  the predicted known class, and  $\mathbb{I}[\cdot]$  the indicator function. The fundamental probabilities—true positive rate (TPR), false positive rate (FPR), and correct classification rate

**Table 1 Target- and source-domain comparison in the main cross-receiver open-set setting.**

Method	Known $\uparrow$	AUROC $\uparrow$	OSCR $\uparrow$	FPR <sub>90</sub> $\downarrow$
<i>Target-domain test</i>				
Target-supervised MSP (Hendrycks and Gimpel, 2016)	<b>0.9610<math>\pm</math>0.0074</b>	0.9254 $\pm$ 0.0157	0.9057 $\pm$ 0.0175	0.2134 $\pm$ 0.0606
Target-supervised OpenMax (Bendale and Boulton, 2016)	0.7664 $\pm$ 0.0142	0.8328 $\pm$ 0.0145	0.7434 $\pm$ 0.0129	0.7579 $\pm$ 0.0492
MeDAE (Huang et al., 2025)	0.8449 $\pm$ 0.0319	0.9521 $\pm$ 0.0159	0.9313 $\pm$ 0.0252	0.1004 $\pm$ 0.0657
PCPD (Hong et al., 2026)	0.4365 $\pm$ 0.1146	0.8557 $\pm$ 0.0262	0.6668 $\pm$ 0.2260	0.4638 $\pm$ 0.0520
FTAN (Xiao et al., 2025)	0.8867 $\pm$ 0.0330	0.9070 $\pm$ 0.0186	0.8749 $\pm$ 0.0264	0.2976 $\pm$ 0.0767
DANN+Weibull (Liu et al., 2025)	0.9005 $\pm$ 0.0210	0.8905 $\pm$ 0.0329	0.8685 $\pm$ 0.0364	0.2970 $\pm$ 0.0849
CRODA-ST	0.9092 $\pm$ 0.0192	<b>0.9692<math>\pm</math>0.0099</b>	<b>0.9580<math>\pm</math>0.0123</b>	<b>0.0469<math>\pm</math>0.0310</b>
<i>Source-domain test</i>				
Target-supervised MSP (Hendrycks and Gimpel, 2016)	<b>0.9806<math>\pm</math>0.0092</b>	0.9335 $\pm$ 0.0233	0.9246 $\pm$ 0.0256	0.1509 $\pm$ 0.0468
Target-supervised OpenMax (Bendale and Boulton, 2016)	0.8851 $\pm$ 0.0173	0.9129 $\pm$ 0.0167	0.8661 $\pm$ 0.0194	0.2572 $\pm$ 0.1443
MeDAE (Huang et al., 2025)	0.9451 $\pm$ 0.0089	<b>0.9808<math>\pm</math>0.0075</b>	<b>0.9726<math>\pm</math>0.0113</b>	0.0268 $\pm$ 0.0225
PCPD (Hong et al., 2026)	0.5662 $\pm$ 0.3303	0.8183 $\pm$ 0.1776	0.6659 $\pm$ 0.3670	0.3900 $\pm$ 0.3450
FTAN (Xiao et al., 2025)	0.9357 $\pm$ 0.0067	0.9358 $\pm$ 0.0136	0.9245 $\pm$ 0.0157	0.1464 $\pm$ 0.0518
DANN+Weibull (Liu et al., 2025)	0.9297 $\pm$ 0.0189	0.9194 $\pm$ 0.0296	0.9025 $\pm$ 0.0337	0.2120 $\pm$ 0.0965
CRODA-ST	0.9443 $\pm$ 0.0092	0.9794 $\pm$ 0.0073	0.9724 $\pm$ 0.0090	<b>0.0261<math>\pm</math>0.0141</b>

*Note:* All methods follow the same deployment-constrained protocol: source training, the same 20 labeled target enrollment samples per class, and threshold/model selection without access to target-test or target-unknown samples. Target-supervised MSP uses source and labeled target CE only; target-supervised OpenMax uses the same allowed known training/enrollment samples for OpenMax fitting. OSCR: open-set classification rate; FPR<sub>90</sub>: false positive rate at 90% true positive rate.

(CCR)—are formulated as follows:

$$\begin{aligned}
\text{Acc}_K &= \frac{1}{|\mathcal{D}_K|} \sum_{(x,y) \in \mathcal{D}_K} \mathbb{I}[\hat{k}(x) = y], \\
\text{TPR}(\gamma) &= \frac{1}{|\mathcal{D}_K|} \sum_{x \in \mathcal{D}_K} \mathbb{I}[s(x) \geq \gamma], \\
\text{FPR}(\gamma) &= \frac{1}{|\mathcal{D}_U|} \sum_{x \in \mathcal{D}_U} \mathbb{I}[s(x) \geq \gamma], \\
\text{CCR}(\gamma) &= \frac{1}{|\mathcal{D}_K|} \sum_{(x,y) \in \mathcal{D}_K} \mathbb{I}[\hat{k}(x) = y, s(x) \geq \gamma].
\end{aligned} \tag{12}$$

AUROC integrates the area under the (FPR( $\gamma$ ), TPR( $\gamma$ )) curve, whereas OSCR integrates the (FPR( $\gamma$ ), CCR( $\gamma$ )) curve to jointly evaluate classification and rejection. The strict metric FPR<sub>90</sub> is defined as FPR( $\gamma_{90}$ ) where TPR( $\gamma_{90}$ ) = 0.90. Note that the swept threshold  $\gamma$  is used solely for continuous score-separation analysis. In actual deployment, the inference threshold  $\tau$  is strictly calibrated on source validation samples without exposing target unknowns.

## 4.2 Overall Cross-Receiver Comparison

The main comparison evaluates the recognition–rejection tradeoff under unknown-free calibration against open-set modeling, fine-tuning, and domain-adaptation baselines. As shown in Table 1, CRODA-ST successfully resolves this tradeoff under cross-receiver conditions. It provides a structurally robust rejection boundary where deep baselines otherwise fail.

Specifically, target-supervised MSP and MeDAE achieve high known-class accuracy on the target domain (0.9610 and 0.8449, respectively). This confirms that minimal target enrollment effectively repairs closed-set recognition. However, their high false positive rates (FPR<sub>90</sub> of 0.2134 and 0.1004) expose a critical failure mode in IoT authentication. Closed-set supervision artificially inflates prediction confidence, but it fails to establish reliable geometric boundaries for unknown rejection when receiver shift distorts the RF fingerprint manifold. Conversely, post-hoc calibration and prototype-based methods (OpenMax and PCPD) suffer severe accuracy drops on the target domain. This demonstrates that mathematical recalibration directly breaks down if the target feature space is not explicitly anchored.

By contrast, CRODA-ST explicitly structures the target feature space prior to rejection. It reduces the target FPR<sub>90</sub> to 0.0469 while retaining a highly competitive 0.9092 known-class accuracy. This substantial drop in false-acceptance risk is accompanied by stable source-domain preservation (FPR<sub>90</sub> of 0.0261). Therefore, the comparison confirms a key mechanism: target-domain known-class supervision alone is insufficient for open-set safety. Cross-receiver structure alignment is fundamentally necessary to suppress condition-dependent confidence artifacts.

**Table 2 Robustness on 10 randomly selected source-target receiver pairs.**

Pair	Known $\uparrow$	OSCR $\uparrow$	FPR <sub>90</sub> $\downarrow$
1-1 $\rightarrow$ 14-7	0.9109	0.9383	0.0952
7-14 $\rightarrow$ 19-2	0.8907	0.9153	0.1419
1-1 $\rightarrow$ 7-7	0.9087	0.9406	0.1029
14-7 $\rightarrow$ 1-1	0.9502	0.9567	0.0642
1-1 $\rightarrow$ 1-19 $\uparrow$	0.9092	0.9580	0.0469
20-19 $\rightarrow$ 19-1	0.9367	0.9463	0.0736
14-7 $\rightarrow$ 19-1	0.9285	0.9336	0.1182
14-7 $\rightarrow$ 20-1	0.8739	0.8867	0.2354
1-1 $\rightarrow$ 20-1	0.8565	0.8641	0.2815
7-7 $\rightarrow$ 20-19	0.9251	0.9331	0.1246

Note: Each non-canonical pair is averaged over 9 runs.  $\uparrow$  uses the canonical result in Table 1. OSCR: open-set classification rate; FPR<sub>90</sub>: false positive rate at 90% true positive rate.

**Table 3 Target-domain ablation of DSA and ROA in the canonical setting.**

Setting	Known $\uparrow$	OSCR $\uparrow$	FPR <sub>90</sub> $\downarrow$
DSA w/o ROA	0.8512	0.8996	0.2360
ROA w/o DSA	0.1483	0.2300	0.6021
TARGET CLASS ANCHORING	0.8394	0.8755	0.2970
CROSS-RECEIVER CONTRAST	0.3520	0.7956	0.4524
FULL DSA	0.8512	0.8996	0.2360
DSA+RECEIVER ALIGNMENT	0.8774	0.9102	0.1975
DSA+LOCAL SMOOTHING	0.8629	0.9156	0.1627
FULL CRODA-ST	<b>0.9092</b>	<b>0.9580</b>	<b>0.0469</b>

Note: The full-model row reports the target-domain CRODA-ST means from Table 1; AUROC is omitted in this ablation table. Note that FULL DSA is functionally equivalent to DSA w/o ROA, combining both Target Class Anchoring ( $\mathcal{L}_T$ ) and Cross-Receiver Contrast ( $\mathcal{L}_{sup}$ ). OSCR: open-set classification rate; FPR<sub>90</sub>: false positive rate at 90% true positive rate.

### 4.3 Robustness on Canonical and Random Pairs

To verify whether this structural alignment generalizes beyond a specific hardware combination, Table 2 reports the robustness across 10 randomly selected source-target receiver pairs. The results demonstrate that the target known-class anchoring and rejection capabilities of CRODA-ST generalize comprehensively across diverse hardware shifts.

Across these 10 random configurations, CRODA-ST consistently maintains high known-class recovery (accuracy  $> 0.8565$ ) while effectively bounding the false acceptance risk (with  $FPR_{90} \leq 0.1419$  on most pairs). The primary performance variation concentrates at the open-set rejection boundary rather than the closed-set recognition rate. For the two most challenging receiver pairs, the  $FPR_{90}$  rises to 0.2354 and 0.2815. This indicates a physical limitation: when severe hardware distortion heavily compresses the margin between known and unknown transmitters, false acceptance remains the dominant residual challenge.

### 4.4 Ablation and Mechanism Verification

Component-level ablation experiments, detailed in Table 3, reveal that structural repair (DSA) and receiver-oriented regularization (ROA) are funda-

mentally interdependent. Neither mechanism alone can solve the cross-receiver open-set problem.

Applying ROA without a prior target-anchored structure causes severe known-class collapse, plunging the accuracy to 0.1483. Naive domain alignment destructively merges unanchored target semantics. Conversely, applying DSA alone successfully restores known-class accuracy to 0.8512 but leaves a substantial false acceptance gap ( $FPR_{90}$  of 0.2360).

Breaking down the DSA stage further clarifies the underlying mechanism. Target class anchoring supplies the necessary spatial references, while cross-receiver contrast securely ties these references to the source geometry. Only when DSA establishes this compact, target-anchored feature space can the subsequent receiver-adversarial alignment and local posterior smoothing safely shrink the known-class boundaries to reject unknowns (dropping  $FPR_{90}$  to 0.0469). This structural dependency confirms that the components are sequentially necessary, rather than merely additive, to unlock the final rejection capacity.

The target feature-space visualization provides a direct embedding-level counterpart to the ablation results. As illustrated in Fig. 3, explicitly structuring the target-known space directly mitigates false acceptance. The DSA stage successfully localizes target known-class clusters. Subsequently, the full objective further tightens these distributions, significantly reducing the density of unknown samples near high-confidence known regions. Thus, the reduction in  $FPR_{90}$  is not merely a score-level scaling artifact. It is grounded in a physical feature-space pattern where known transmitters are compacted and unknown samples are systematically expelled from confident acceptance zones.

### 4.5 Temporal Shift, Openness, and Cost

The final analysis demonstrates that CRODA-ST's cross-receiver mechanisms provide collateral robustness against temporal shift and varying openness, while retaining a lightweight online authentication path.

Under a severe few-shot diagnostic setting (Table 4), CRODA-ST maintains stable recognition and rejection across time captures. With 4 labeled and 4 unlabeled target-known auxiliary samples, the cross-day target known accuracy reaches 0.8125, which tightly tracks the same-day performance of 0.8153.

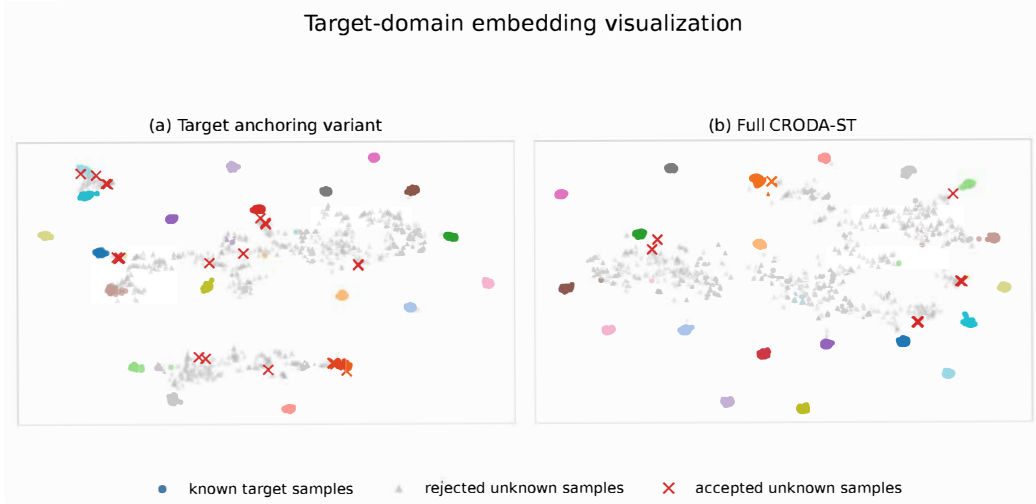


**Fig. 3** Target-domain t-distributed stochastic neighbor embedding (t-SNE) visualization in the canonical 1-1→1-19 setting. Colored circles represent sampled known target classes, gray triangles indicate successfully rejected unknown samples, and red crosses denote false-positive accepted unknown samples. CRODA-ST forms more compact known-class clusters and leaves fewer unknown samples in high-confidence known regions.

**Table 4** Target-domain adaptation and source-domain preservation under same-day and cross-day target data.

Domain L/U	Same-day		Cross-day	
	Known	OSCR	Known	OSCR
Target 2/6	0.7017±0.0442	0.7753±0.0287	0.6772±0.0426	0.7415±0.0173
Target 3/5	0.7806±0.0262	0.8370±0.0205	0.7467±0.0423	0.7855±0.0203
Target 4/4	0.8153±0.0177	0.8489±0.0155	0.8125±0.0259	0.8284±0.0217
Source 2/6	0.9441±0.0152	0.9492±0.0147	0.9405±0.0118	0.9465±0.0153
Source 3/5	0.9508±0.0126	0.9577±0.0137	0.9435±0.0109	0.9469±0.0139
Source 4/4	0.9479±0.0071	0.9490±0.0114	0.9443±0.0099	0.9481±0.0157

*Note:* L/U denotes labeled/unlabeled auxiliary samples from target known classes. This table reports a diagnostic variant rather than the main deployment protocol: the U samples are used only as unlabeled target-domain data for receiver-discrimination and VAT regularization, and their labels are not used for target CE, supervised contrastive learning, threshold calibration, or model selection. Source rows use the held-out source test split.

**Table 5** Sensitivity to openness in the 1-1→1-19 setting.

Open.	$K_{tr}/K_{te}$	Known ↑	OSCR ↑	FPR <sub>90</sub> ↓
0.10	81/119	0.9051±0.0140	0.9318±0.0104	0.1138±0.0413
0.19	64/133	0.9193±0.0159	0.9467±0.0171	0.0764±0.0397
0.30	37/114	0.9092±0.0192	<b>0.9580±0.0123</b>	<b>0.0469±0.0310</b>
0.40	27/123	0.8793±0.0215	0.9244±0.0168	0.1640±0.0697
0.50	19/133	0.9275±0.0247	0.9520±0.0173	0.0957±0.0403
0.59	12/133	<b>0.9564±0.0406</b>	0.9386±0.0450	0.1391±0.1070

*Note:*  $K_{tr}/K_{te}$  denotes known training classes / total test classes.

**Table 6** Online inference cost of CRODA-ST in the canonical cross-receiver setting.

Online model	Params	Storage	MACs	CPU latency
2-D residual encoder + linear classifier	0.262M	1.05 MB	5.29M	1.35 ms/sample

*Note:* Costs are measured for one  $2 \times 256$  I/Q sample with 37 known classes. MACs count one multiply-accumulate as one operation, corresponding to approximately 10.48M FLOPs under a two-operation multiply-add convention. Latency is averaged over 800 CPU forward passes using one PyTorch thread on an Intel Core i9-12900HX. With batch size 64, the amortized latency is 0.51 ms per sample.

This validates that the structured feature space is resilient to daily channel and phase variations.

Furthermore, the openness sensitivity analysis (Table 5) uncovers a critical operational dynamic. The rejection capacity does not degrade strictly

monotonically as the number of unknown classes increases. Instead, the false acceptance risk (FPR<sub>90</sub>) is driven by the specific hardware-fingerprint overlap between the known manifold and the newly introduced unknown identities, rather than the sheer volume of unknown classes.

Table 6 quantifies the online cost of CRODA-ST. At deployment, each I/Q segment is passed once through the 2-D residual encoder and the linear classifier, and open-set rejection is performed by comparing the maximum softmax probability with the source-calibrated threshold. The receiver discriminator, VAT perturbation, and supervised contrastive objective are used only as training-time constraints and are removed from online authentication. Therefore, CRODA-ST introduces no additional online model branch beyond the standard encoder-classifier path.

The resulting model contains only 0.262M trainable parameters and requires 5.29M MACs for a  $2 \times 256$  I/Q sample. Its FP32 parameter storage is approximately 1.05 MB, and the measured single-thread CPU latency is merely 1.35 ms per sample. These results validate that the enhanced cross-receiver open-set safety is achieved via a lightweight receiver-side inference path rather than relying on costly generative or post-hoc online modules, fully satisfying the stringent resource constraints of practical IoT deployment.

**Table 7 Target- and source-domain open-set performance on selected LoRa receiver pairs.**

Receiver Pair	Known $\uparrow$	AUROC $\uparrow$	OSCR $\uparrow$	FPR <sub>90</sub> $\downarrow$
<i>Target-domain test</i>				
LoRa-5 $\rightarrow$ LoRa-1	0.9620	0.9452	0.9452	0.0962
LoRa-7 $\rightarrow$ LoRa-3	0.9780	0.9416	0.9416	0.1514
LoRa-9 $\rightarrow$ LoRa-4	0.9840	0.9310	0.9310	0.1090
LoRa-4 $\rightarrow$ LoRa-6	0.9940	0.9226	0.9226	0.1600
LoRa-9 $\rightarrow$ LoRa-6	1.0000	0.9225	0.9225	0.1295
<i>Target Mean</i>	<b>0.9836</b>	<b>0.9326</b>	<b>0.9326</b>	<b>0.1292</b>
<i>Source-domain test (Preservation)</i>				
LoRa-5 $\rightarrow$ LoRa-1	0.9950	0.9860	0.9855	0.0285
LoRa-7 $\rightarrow$ LoRa-3	0.9960	0.9812	0.9810	0.0310
LoRa-9 $\rightarrow$ LoRa-4	0.9980	0.9895	0.9890	0.0210
LoRa-4 $\rightarrow$ LoRa-6	0.9970	0.9840	0.9835	0.0260
LoRa-9 $\rightarrow$ LoRa-6	1.0000	0.9910	0.9910	0.0180
<i>Source Mean</i>	<b>0.9972</b>	<b>0.9863</b>	<b>0.9860</b>	<b>0.0249</b>

*Note:* Results report open-set performance under source-calibrated thresholding. Target rows evaluate open-set classification on the target receiver, while source rows confirm identity preservation on the original source receiver. OSCR: open-set classification rate; FPR<sub>90</sub>: false positive rate at 90% true positive rate.

#### 4.6 Evaluation on Controllable LoRa Simulation Array

To provide complementary validation beyond the WiFi dataset, we evaluate CRODA-ST on a synthetic LoRa protocol with ten systematically controlled receiver hardware configurations (LoRa-1 to LoRa-10). Table 7 reports selected cross-receiver transfer pairs across both target and source test domains.

As shown in Table 7, the LoRa simulation array provides a complementary cross-protocol check for CRODA-ST under explicit hardware impairments. On the target domain, CRODA-ST achieves a mean FPR<sub>90</sub> of 0.1292 together with a mean known-class accuracy of 0.9836. These results indicate that the source-calibrated open-set formulation remains usable beyond the WiFi measurement protocol. Concurrently, CRODA-ST preserves near-perfect identity structures on the source domain (mean known accuracy 0.9972), suggesting that target-side regularization does not destructively interfere with the original representation capacity.

## 5 Conclusion

This study investigated the single-source single-target cross-receiver open-set RFFI challenge, addressing the critical deployment mismatch where a target receiver simultaneously confronts shifted known transmitters and unseen rogue devices under a source-calibrated threshold. We demonstrated that standard closed-set adaptation models suffer from severe confidence inflation, inherently compromising open-set authentication. To resolve this, we proposed CRODA-ST, recasting the recognition–rejection tradeoff as a threshold-

reliability problem. Its structure-first design integrates target known-class anchoring (DSA) with rejection-oriented receiver regularization (ROA), ensuring that the source-calibrated boundary remains structurally intact without exposing target-unknown samples during training.

Extensive evaluations on the WiSig ManyTx dataset confirm that CRODA-ST effectively reduces the false acceptance risk (yielding an FPR<sub>90</sub> of 0.0469) while preserving strong target known-class recognition (0.9092 accuracy). Complementary evaluations on a controllable LoRa simulation array provide a cross-protocol check under synthesized hardware distortions. Furthermore, our ablation and visualization results indicate a key mechanistic dependency: receiver regularization mitigates false acceptance only after target known classes are explicitly anchored. Subsequent temporal and openness analyses show that the framework maintains resilient identity separation beyond the canonical training conditions, though extreme hardware-fingerprint overlap remains a fundamental boundary. Overall, CRODA-ST provides a structurally sound paradigm for cross-receiver RFFI, suppressing condition-dependent confidence artifacts to support source-calibrated rejection in heterogeneous IoT networks.

## References

- Bendale A, Boulton TE, 2016. Towards open set deep networks. 2016 IEEE Conference on Computer Vision and Pattern Recognition (CVPR), p.1563-1572. <https://doi.org/10.1109/CVPR.2016.173>
- Cai Z, Wang Y, Jiang Q, et al., 2024. Toward intelligent lightweight and efficient uav identification with rf fingerprinting. *IEEE Internet of Things Journal*, 11(15):26329-26339. <https://doi.org/10.1109/JIOT.2024.3395466>
- Chen G, Peng P, Wang X, et al., 2021. Adversarial reciprocal points learning for open set recognition. *IEEE Transactions on Pattern Analysis and Machine Intelligence*, 44(11):8065-8081. <https://doi.org/10.1109/TPAMI.2021.3106743>
- Chillet A, Gerzaguet R, Desnos K, et al., 2024. Understanding radio frequency fingerprint identification with rifyfi virtual databases. *IEEE Open Journal of the Communications Society*, 5:2076-2091. <https://doi.org/10.1109/OJCOMS.2024.3414858>
- Feng J, Fang S, Fan Y, 2025. Cross-receiver radio frequency fingerprint identification based on domain adaptation with dynamic distribution alignment. *IEEE Internet of Things Journal*, 12(16):33202-33214. <https://doi.org/10.1109/JIOT.2025.3573713>
- Ganin Y, Ustinova E, Ajakan H, et al., 2016. Domain-adversarial training of neural networks. *Journal of Machine Learning Research*, 17(59):1-35.

- Gao Y, Ma AJ, Gao Y, et al., 2020. Adversarial open set domain adaptation via progressive selection of transferable target samples. *Neurocomputing*, 411:290-297. <https://doi.org/10.1016/j.neucom.2020.05.032>
- Geng C, Huang SJ, Chen S, 2021. Recent advances in open set recognition: A survey. *IEEE Transactions on Pattern Analysis and Machine Intelligence*, 43(10):3614-3631. <https://doi.org/10.1109/TPAMI.2020.2981604>
- Guo L, Liu C, Liu Y, et al., 2024. Toward open-set specific emitter identification using auxiliary classifier generative adversarial network and openmax. *IEEE Transactions on Cognitive Communications and Networking*, 10(6):2019-2028. <https://doi.org/10.1109/TCCN.2024.3408417>
- Hanna S, Karunaratne S, Cabric D, 2022. Wisig: A large-scale wifi signal dataset for receiver and channel agnostic rf fingerprinting. *IEEE Access*, 10:22808-22818. <https://doi.org/10.1109/ACCESS.2022.3154790>
- Hendrycks D, Gimpel K, 2016. A baseline for detecting misclassified and out-of-distribution examples in neural networks. arXiv preprint arXiv:161002136, p.1-5. <https://doi.org/10.48550/arXiv.1610.02136>
- Hong Z, Lin J, Li T, et al., 2026. Open-set domain adaptive rf fingerprint identification based on prototype calibration. *IEEE Wireless Communications Letters*, 15:775-779. <https://doi.org/10.1109/LWC.2025.3638380>
- Huang R, Peng X, Chai Z, et al., 2024. Radio frequency fingerprint extraction and authentication towards open set in noisy channels. *Digital Signal Processing*, 146:104363. <https://doi.org/10.1016/j.dsp.2023.104363>
- Huang S, Guo L, Fu X, et al., 2025. Open-set specific emitter identification leveraging enhanced metric denoising autoencoders. *IEEE Internet of Things Journal*, 12(4):3453-3462. <https://doi.org/10.1109/JIOT.2024.3404042>
- Kangsheng L, Wenjun Y, Limin Z, et al., 2026. An open-set communication-specific emitter identification method based on adaptive weibull hierarchical decision. *IEEE Internet of Things Journal*, Early Access(1):1-1. <https://doi.org/10.1109/JIOT.2026.3655345>
- Li K, Bao J, Xie X, et al., 2025. Receiver-agnostic radio frequency fingerprint identification for zero-trust wireless networks. *IEEE Journal on Selected Areas in Communications*, 43(6):1981-1997. <https://doi.org/10.1109/JSAC.2025.3560002>
- Liu X, Luo Z, Shang J, 2025. Open-set specific emitter identification under cross-receiver conditions. 2025 17th International Conference on Communication Software and Networks (ICCSN), Qingdao, China, p.216-222. <https://doi.org/10.1109/ICCSN66511.2025.11172556>
- Loghmani MR, Vincze M, Tommasi T, 2020. Positive-unlabeled learning for open set domain adaptation. *Pattern Recognition Letters*, 136:213-219. <https://doi.org/10.1016/j.patrec.2020.06.003>
- Ma J, Zhang J, Shen G, et al., 2025a. Toward channel-robust and receiver-independent radio frequency fingerprint identification. *IEEE Transactions on Information Forensics and Security*, 20:1132-1146. <https://doi.org/10.1109/TIFS.2025.3630316>
- Ma Z, Fang S, Fan Y, 2025b. Open-set radio frequency fingerprint identification method based on multi-task prototype learning. *Sensors*, 25(17):5415. <https://doi.org/10.3390/s25175415>
- Miyato T, Maeda Si, Koyama M, et al., 2018. Virtual adversarial training: A regularization method for supervised and semi-supervised learning. *IEEE Transactions on Pattern Analysis and Machine Intelligence*, 41(8):1979-1993. <https://doi.org/10.1109/TPAMI.2018.2858821>
- Peng L, Hu A, Zhang J, et al., 2019. Design of a hybrid rf fingerprint extraction and device classification scheme. *IEEE Internet of Things Journal*, 6(1):349-360. <https://doi.org/10.1109/JIOT.2018.2838071>
- Peng L, Peng H, Fu H, et al., 2024. Channel-robust radio frequency fingerprint identification for cellular uplink lte devices. *IEEE Internet of Things Journal*, 11(16):27440-27451. <https://doi.org/10.1109/JIOT.2024.3358904>
- Qi X, Hu A, Chen T, 2024. Lightweight radio frequency fingerprint identification scheme for v2x based on temporal correlation. *IEEE Transactions on Information Forensics and Security*, 19:1056-1070. <https://doi.org/10.1109/TIFS.2023.3329683>
- Sa K, Lang D, Wang C, et al., 2019. Specific emitter identification techniques for the internet of things. *IEEE Access*, 8:1644-1652. <https://doi.org/10.1109/ACCESS.2019.2962626>
- Shen G, Zhang J, Marshall A, et al., 2022. Towards scalable and channel-robust radio frequency fingerprint identification for lora. *IEEE Transactions on Information Forensics and Security*, 17:774-787. <https://doi.org/10.1109/TIFS.2022.3152404>
- Shen G, Zhang J, Marshall A, et al., 2024. Towards receiver-agnostic and collaborative radio frequency fingerprint identification. *IEEE Transactions On Mobile Computing*, 23(7):7618-7634. <https://doi.org/10.1109/TMC.2023.3340039>
- Wang J, 2021. Exploring category attention for open set domain adaptation. *IEEE Access*, 9:37223-37232. <https://doi.org/10.1109/ACCESS.2021.3049552>
- Wang J, Wang H, Wang W, et al., 2025a. Os-sei: Open-set specific emitter identification based on outlier exposure and label smoothing. *IEEE Internet of Things Journal*, Early Access(1):1-1. <https://doi.org/10.1109/JIOT.2025.3560233>
- Wang Q, Sun Y, Wang Z, et al., 2025b. Model-based rf fingerprint extraction approach for robust iot device identification. *IEEE Internet of Things Journal*, 12:21915-21930. <https://doi.org/10.1109/jiot.2025.3549231>
- Xiao Z, Zhang X, Sun G, et al., 2025. Ftan: Feature transform and alignment network for cross-domain specific emitter identification. *Signal Processing*, 230:109800. <https://doi.org/10.1016/j.sigpro.2024.109800>
- Xing Y, Hu A, Zhang J, et al., 2023. Design of a channel robust radio frequency fingerprint identification scheme. *IEEE Internet of Things Journal*, 10(8):6946-6959. <https://doi.org/10.1109/JIOT.2022.3228280>
- Xing Y, Zhang X, Li G, et al., 2025. A robust radio frequency fingerprint open-set recognition scheme for iot devices. *IEEE Transactions On Information Forensics*

- and Security*, 20:12693-12706.  
<https://doi.org/10.1109/TIFS.2025.3636021>
- Yan G, Fu X, Wang Y, et al., 2025. Radio frequency fingerprint identification towards statistical and deep learning features: Review, recent results and future directions. *Peer-to-Peer Networking and Applications*, 18(3):116.  
<https://doi.org/10.1007/s12083-024-01902-9>
- Yang J, Feng S, Wang Y, et al., 2025a. Openrfi: Open-set radio frequency fingerprint identification via test-time fine-tuning. *IEEE Transactions on Mobile Computing*, 24(11):10596-10610.  
<https://doi.org/10.1109/TMC.2025.3582980>
- Yang J, Zhu S, Wen Z, et al., 2025b. Cross-receiver radio frequency fingerprint identification: A source-free adaptation approach. *Sensors*, 25(14):4451.  
<https://doi.org/10.3390/s25144451>
- Yang L, Li Q, Ren X, et al., 2024. Mitigating receiver impact on radio frequency fingerprint identification via domain adaptation. *IEEE Internet of Things Journal*, 11(17):28780-28792.  
<https://doi.org/10.1109/JIOT.2024.3389491>
- Zha X, Li T, Qiu Z, et al., 2023. Cross-receiver radio frequency fingerprint identification based on contrastive learning and subdomain adaptation. *IEEE Signal Processing Letters*, 30:266-270.  
<https://doi.org/10.1109/LSP.2023.3241592>
- Zhang J, Shen G, Saad W, et al., 2023. Radio frequency fingerprint identification for device authentication in the internet of things. *IEEE Communications Magazine*, 61(10):110-115.  
<https://doi.org/10.1109/MCOM.003.2200974>
- Zhang Y, Li Q, Liu H, et al., 2025. Domain generalization for cross-receiver radio frequency fingerprint identification. *IEEE Internet of Things Journal*, 12(10):17881-17893.  
<https://doi.org/10.1109/JIOT.2024.3486068>
- Zhao X, Wang S, Sun Q, 2023. Open-set domain adaptation by deconfounding domain gaps. *Applied Intelligence*, 53(10):12208-12224.  
<https://doi.org/10.1007/s10489-022-03805-9>